15
Some fundamental measurements

This final chapter has three goals. First, we want to show how experimentalists have measured properties of subatomic particles. This section takes the form of a survey of some of the applicable techniques. Second, we want to discuss some of the considerations involved in measurements of particle interactions, such as total cross sections, elastic differential cross sections, polarization experiments, and new particle searches. Finally, we want to illustrate these measurements with examples of actual particle physics experiments.

15.1 Particle properties

In this section we will describe some of the methods used to measure the basic properties of the elementary particles. As mentioned in Chapter 1, these properties include charge, mass, spin, magnetic moment, lifetime, and branching ratios. Many specialized techniques have been developed for measuring some of these properties, particularly for the electron and nucleons. We will not attempt to survey all the applicable procedures for each particle, since many of the methods use techniques from atomic and molecular physics that fall outside the scope of this book. Instead we will follow the philosophy of the preceding chapters and discuss selected examples in more detail.

15.1.1 Charge

The sign of a particle's charge may be inferred from the direction of its deflection (if any) in a magnetic field of known orientation. The magnitude of the charge can be determined if the momentum of the particle and the strength of the magnetic field are known. Deflection in an electric field could also be used, although this is not so useful for high energy particles.

https://doi.org/10.1017/9781009290098.016 Published online by Cambridge University Press

An alternative method for measuring the magnitude of a particle's charge is to measure a charge dependent quantity, such as the ionization energy loss or the Rutherford scattering cross section. This method has been used in a free quark search to measure the masses of particles produced in e^+e^- collisions [1]. The energy loss was sampled in selected scintillation counters, whereas the time of flight of the particle was measured in some others. Combining the value of β from the time of flight counters with the mean value of dE/dx allows the charge to be calculated from the Bethe–Bloch equation. The system calibration was provided by cosmic rays.

15.1.2 Mass

Many specialized techniques have been used to determine the masses of particles. For example, the π^- and K^- masses have been determined from the photons emitted in pionic and kaonic atoms [2]. The muon mass has been measured in the "g-2" spin procession experiments [3, 4].

A common method is to measure two independent kinematic quantities involving the mass of the particle. One of these quantities is usually the momentum, since it can easily be measured using a spectrometer. The other quantity could be the ionization, range, or velocity. The velocity could in turn be calculated from the results of a dE/dx, Cerenkov, or time of flight measurement. The laws of conservation of energy and momentum could then be used to calculate the mass of the particle. Källén [4] has given a nice summary of particle mass measurements.

As an example of a mass measurement consider the experiment of Daum et al. [5], which placed an upper limit on the mass of the muon neutrino from a study of $\pi^+ \rightarrow \mu^+ \nu_\mu$ decays at rest. Energy and momentum conservation give ($c = 1$)

$$m_\pi = \sqrt{p^2 + m_\mu^2} + \sqrt{p^2 + m_\nu^2}$$

where p is the momentum of the decay muon. The ν_μ mass can then be calculated from

$$m_\nu^2 = m_\pi^2 + m_\mu^2 - 2m_\pi (p^2 + m_\mu^2)^{1/2}$$

The error in the squared mass arising from an error in the momentum measurement is

$$\delta(m_\nu^2) = \frac{2m_\pi p}{\sqrt{p^2 + m_\mu^2}} \delta p \approx 76\, \delta p$$

since p is known to be around 30 MeV. The errors due to the uncertainties in the π^+ and μ^+ masses contribute similar amounts. Thus, a measure-

https://doi.org/10.1017/9781009290098.016 Published online by Cambridge University Press

ment of the muon momentum with an accuracy of about 0.001 MeV can be combined with prior measurements of the π^+ and μ^+ masses to determine the ν_μ mass with an error of ~ 0.1 MeV^2 on the mass squared.

A π^+ beam was passed through a lucite light guide with a thin 1-mm-thick scintillation counter embedded in the downstream side, as shown in Fig. 15.1. The scintillation counter was in a vacuum chamber located between the gaps of a bending magnet. The magnetic field was such that μ^+ from π^+ decays at rest near the downstream edge of the scintillator could follow a trajectory through a set of collimators to a solid state detector on the other side.

Stopping π^+ deposited 3.6 MeV in the scintillator. A gate signal was generated whenever the PMT signal exceeded a discriminator threshold of 3 MeV. The magnetic field was kept uniform to ± 0.15 G over the region of allowed μ^+ trajectories by shimming the pole faces. The field was

Figure 15.1 Magnetic spectrometer for muon momentum measurement. Some of the important features include (4) MWPC for monitoring the beam profile, (10) pion stop scintillator, (12) accepted muon trajectories, (15) NMR probe, (16) silicon surface barrier detector, and (20) ^{241}Am calibration source. (R. Abela et al., Phys. Lett. 146B: 431, 1984.)

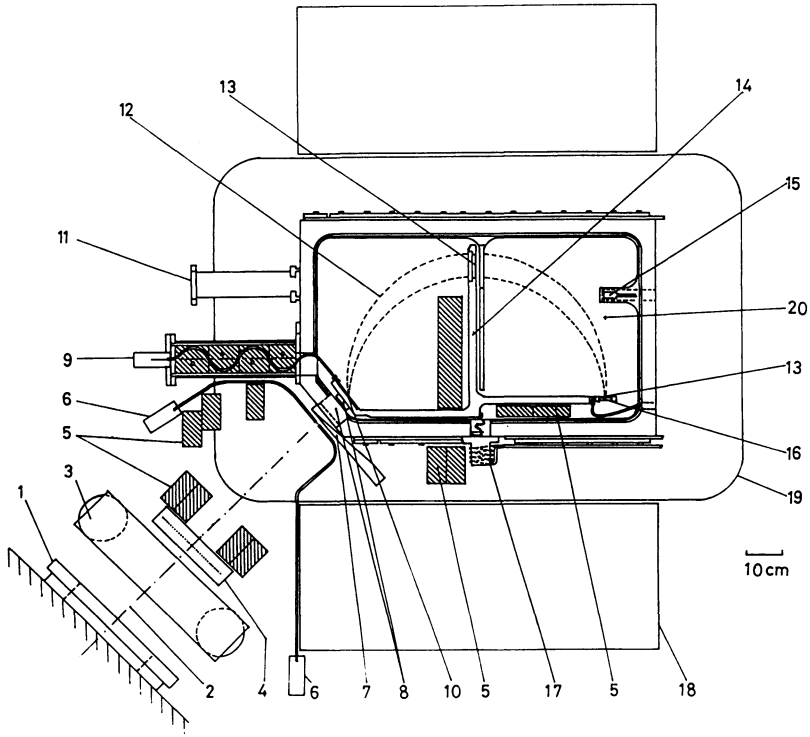

https://doi.org/10.1017/9781009290098.016 Published online by Cambridge University Press

prevented from varying with time using a fixed NMR probe in a feedback circuit with a set of correction coils. The silicon surface detector signal was sent to a pulse height analyzer, which was gated by the stopping π^+ signal from the small scintillation counter. Figure 15.2 shows the gated pulse height spectrum. The peak is due to the μ^+ from stopping π^+. Note the excellent energy resolution obtained with the silicon detector. The shoulder to the right of the peak is due to additional energy losses in the silicon detector from the e^+ in $\mu^+ \rightarrow e^+ \nu_e \bar{\nu}_\mu$ decays.

The good event rate had a sharp cutoff above a certain magnetic field. This effect was used to determine the muon momentum from the very precise measurement of B. The measured value was $p = 29.7914 \pm 0.0008$ MeV/c. This result together with the π^+ and μ^+ masses gives the value $m_\nu^2 = -0.163 \pm 0.080$ MeV^2. This corresponds to an upper limit for the ν_μ mass of 0.25 MeV at the 90% confidence level.

15.1.3 Spin

Many particles have a spin degree of freedom associated with them. According to the laws of quantum mechanics, the magnitude and component of the spin along one fixed direction are quantized. The spin

Figure 15.2 Gated pulse height spectra from the silicon detector. (R. Abela et al., Phys. Lett. 146B: 431, 1984.)

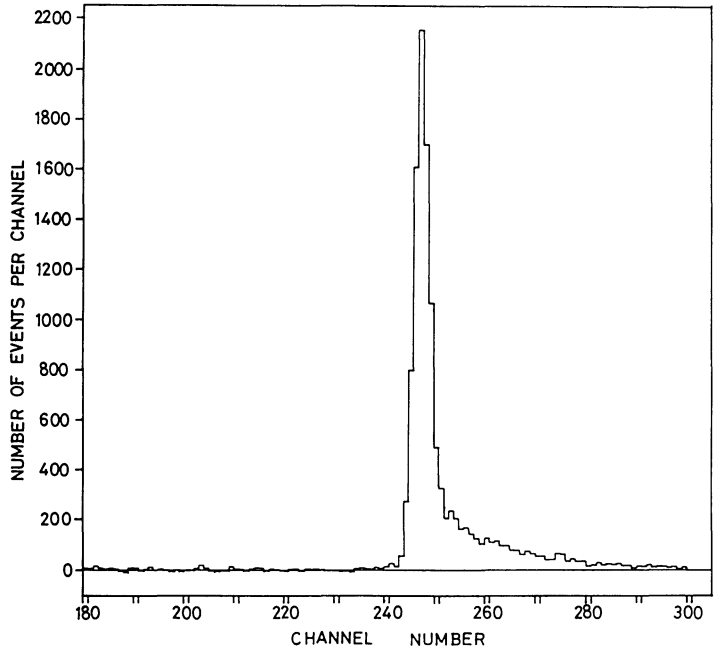

https://doi.org/10.1017/9781009290098.016 Published online by Cambridge University Press

of the particle manifests itself in the decay angular distributions of unstable particles and in the production angular distributions of particle interactions. We will discuss the spin dependence of high energy interactions in more detail in Section 4.

The spins of the electron and nucleons have been determined from the hyperfine structure in optical spectroscopy, from atomic and molecular beam experiments, or from experiments in bulk matter using magnetic resonance techniques [6]. The spins of the charged pions have been determined using the principle of detailed balance, which relates the cross section for a reaction with the cross section for the inverse reaction [7].

15.1.4 Magnetic moment

Closely associated with the spin of a particle is the magnetic moment μ. However, whereas the magnitude of the spin is quantized, the magnitude of the magnetic moment is not. The two quantities are related through the equation

$$\boldsymbol{\mu} = g\mu_{\mathrm{B}}\mathbf{S} \tag{15.1}$$

where μ_{B} is the Bohr magneton and g is an experimental quantity that must be determined for each particle. The Dirac theory predicts that $g = 2$ for pointlike particles.

Any particle possessing a magnetic moment is subject to the force

$$\mathbf{F} = \boldsymbol{\mu}\,\nabla B \tag{15.2}$$

in an inhomogeneous magnetic field. Note that this force is the dominant electromagnetic effect on the motion of a neutral particle. In addition, the magnetic moments of the particles are subject to a torque in a uniform magnetic field given by

$$\mathbf{N} = \boldsymbol{\mu} \times \mathbf{B} \tag{15.3}$$

This torque causes the moment (and spin) to precess in the magnetic field with an angular frequency $\boldsymbol{\Omega}_{\mathrm{s}}$ given in the LAB frame by the Bargmann–Michel–Telegdi equation [8]

$$\boldsymbol{\Omega}_{\mathrm{s}} = \frac{e}{m\gamma}\left[(1 + G)\mathbf{B}_{\parallel} + (1 + G\gamma)\mathbf{B}_{\perp}\right] \tag{15.4}$$

where $\mathbf{B}_{\parallel}$ ($\mathbf{B}_{\perp}$) is the component of $\mathbf{B}$ along (perpendicular to) the particle's velocity, and

$$G = \tfrac{1}{2}(g - 2) \tag{15.5}$$

is the g factor anomaly representing any deviation from pointlike behavior. It follows then that the total precession angle of the moment for a

https://doi.org/10.1017/9781009290098.016 Published online by Cambridge University Press

neutral particle traveling perpendicular to a uniform magnetic field is

$$\phi_p = \frac{e}{m\beta\gamma}(1 + G\gamma)\int B_\perp \, dl \tag{15.6}$$

The momentum of a charged particle will also bend in the magnetic field at the cyclotron frequency

$$\Omega_c = \frac{e}{m\gamma} B_\perp \tag{15.7}$$

Thus, for a charged particle the net angle between the momentum and moment after traversing the field is

$$\phi_{net} = \frac{e}{m\beta} G \int B_\perp \, dl \tag{15.8}$$

We see that for a pointlike charged particle with $G = 0$, the spin precesses at the same rate as the momentum.

The magnetic moments of the electron and nucleons have been determined using atomic physics techniques [6]. The g factor of the muon has been measured in a classic set of storage ring experiments at CERN [3, 9]. A by-product of this effort has been a precise demonstration of the validity of relativistic time dilation.

Schachinger et al. [10] have made a precise measurement of the magnetic moment of the Λ hyperon. The Λ, which were produced inclusively from interactions of a 300-GeV proton beam on a beryllium target at FNAL, had a polarization of $\sim 8\%$. This made it possible to send the Λ through a bending magnet and measure the precession of the net polarization. The amount of precession gives G from Eq. 15.6 and then μ from Eq. 15.1. Good precision was possible since (1) the Λ were produced inclusively with a large cross section, (2) the detector had a large acceptance, and (3) the high energy gives the Λ a long mean decay length.

The experimental arrangement is shown in Fig. 15.3. The proton beam struck the target at a vertical angle. By parity conservation the Λ polarization must be perpendicular to the plane formed by the beam and Λ momenta. Thus, the accepted Λ will have the initial polarization along the $-x$ direction in the figure. The vertical magnetic field causes the direction of the net polarization to precess. A veto counter following the magnet defines the beginning of the Λ decay region. The angle of the polarization after the magnet was determined by measuring the angular distribution of the proton from $\Lambda \rightarrow \pi^- p$ decays. In the Λ rest frame this is given by

$$\frac{1}{N}\frac{dN}{d\Omega} = \frac{1}{4\pi}(1 + \alpha \mathbf{P} \cdot \mathbf{k}) \tag{15.9}$$

https://doi.org/10.1017/9781009290098.016 Published online by Cambridge University Press

where **P** is the Λ polarization vector, **k** is a unit vector along the proton momentum, and $\alpha = 0.647$ is the Λ decay asymmetry parameter.

The precession field was carefully mapped and monitored online using an NMR probe. Many checks were made to minimize any biases. The production angle, precession field, and spectrometer field were all periodically reversed. The precession angle is shown as a function of the integral field in Fig. 15.4. The small background consisted mainly of K^0's, Λ's produced by neutrons interacting in the collimators, and Λ's from Ξ^0 decays. The result for the magnetic moment was $\mu = (-0.6138 \pm 0.0047)\mu_N$.

15.1.5 Lifetime

The relativistic time dilation effect makes it possible to measure the lifetime of an unstable particle by measuring the distribution of its decay points at high energies. We have seen that in the LAB frame this

Figure 15.3 Experimental arrangement for the Λ magnetic moment measurement.

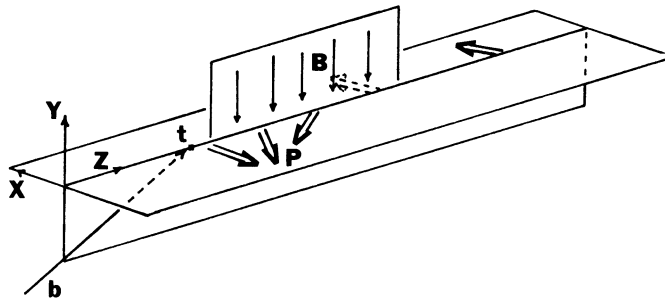

Figure 15.4 Precession angle of the Λ versus the measured field integral. (After L. Schachinger et al., Phys. Rev. Lett. 41: 1348, 1978.)

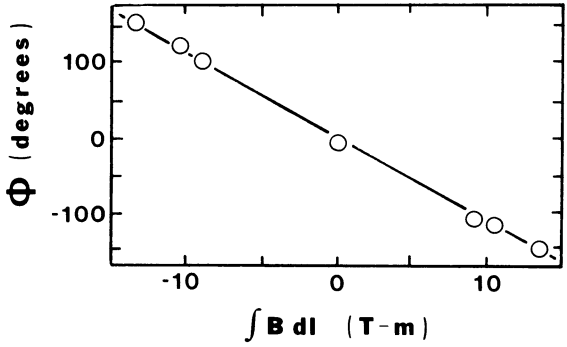

https://doi.org/10.1017/9781009290098.016 Published online by Cambridge University Press

distribution is exponential with a slope that depends on the particle's lifetime. Figure 15.5 shows the experimental arrangement used by Bourquin et al. [11] at the CERN SPS to measure the lifetime of the Ω^- hyperon. The Ω^- were produced by interactions of the primary proton beam in a small target. The trigger for Ω^- in the beam used a DISC Cerenkov counter and was described in Chapter 13. Decays of the type $\Omega^- \rightarrow \Lambda K^-$, $\Lambda \rightarrow \pi^- p$, among others were reconstructed from tracks in the drift chambers. They first selected events containing a Λ by assigning the proton mass to positive tracks and the pion mass to negative tracks and looking for combinations where the effective mass was within 10 MeV of the Λ mass. They then assigned the kaon mass to the other negative track and calculated the ΛK^- effective mass. These events contained a large background of $\Xi^- \rightarrow \Lambda\pi^-$ decays. The Ξ^- decays could be removed by requiring that the effective mass $m(\Lambda\pi^-)$, obtained by interpreting the negative track as a π^-, be larger than 1.350 GeV. Since the Ξ^- mass is 1.321 GeV, this cut removes practically all the true Ξ^- decays, but only about 14% of true Ω^- events. Contamination from $\Omega^- \rightarrow \Xi^0\pi^-$ events was removed by requiring that the sum of the Λ and K^- momenta measured in the spectrometer match within errors the incident Ω^- momentum. The final sample of about 12,000 $\Omega^- \rightarrow \Lambda K^-$ decays had a very clean, narrow peak at the Ω^- mass. Samples of Ξ decays were also collected as a monitor on the experiment.

The Ω^- decay point was reconstructed from the intersection of the Λ and K^- momenta. The decay point distribution for Ω^- events is shown in Fig. 15.6. The solid line represents Monte Carlo calculations that took

Figure 15.5 Experimental apparatus for the Ω^- lifetime measurement. (M. Bourquin et al., Nuc. Phys. B 241: 1, 1984.)

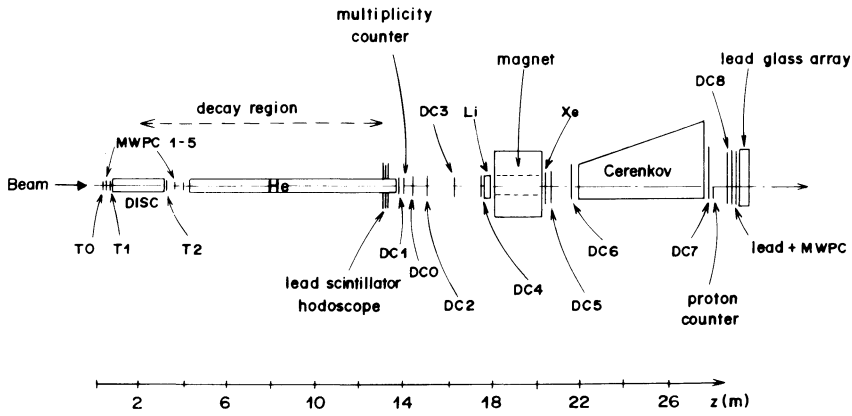

https://doi.org/10.1017/9781009290098.016 Published online by Cambridge University Press

into account various systematic effects. The Ω^- lifetime extracted from the slope was $(0.823 \pm 0.013) \times 10^{-10}$ sec.

15.1.6 *Branching ratios*

Unstable particles generally decay into any combination of other particles that are allowed by energy conservation and are not forbidden by some selection rule. The fraction of the time a particle decays into a specific channel is referred to as its branching ratio. Measurements of branching ratios involve finding the number of events with the desired decay mode, correcting for background and detection efficiencies, and normalizing to the total number of decaying particles, or to one of its principal decay modes. As an example, a measurement of the branching ratio for $\pi^0 \rightarrow \gamma e^+ e^-$ decays is described by Schardt et al. [12].

Figure 15.6 Decay point distribution for $\Omega^- \rightarrow \Lambda K^-$ events. (M. Bourquin et al., Nuc. Phys. B 241: 1, 1984.)

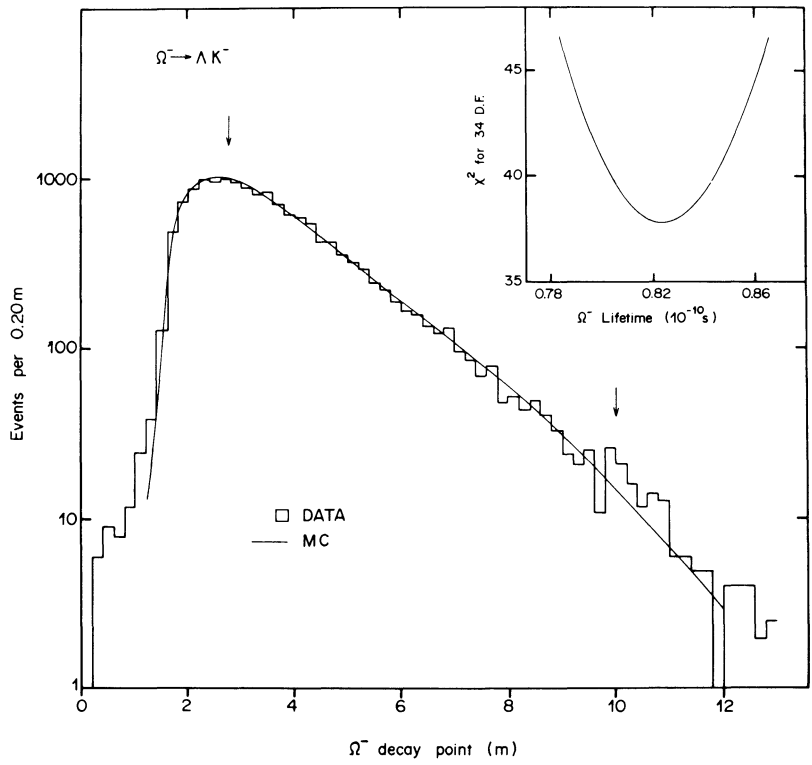

https://doi.org/10.1017/9781009290098.016 Published online by Cambridge University Press

15.2 Total cross section

Two methods are commonly used to directly measure total cross sections. In the first, one attempts to record every interaction that takes place. This requires a detector with $\sim 4\pi$ acceptance. This method is often used for colliding beam experiments. The total cross section is given by

$$\sigma_T = R/\mathscr{L} \tag{15.10}$$

where R is the measured total interaction rate and $\mathscr{L}$ is the measured incident luminosity. A similar procedure is used for bubble chamber experiments. In that case one measures the total number of interactions in some volume of the chamber and normalizes to the number of incident particles.

The second direct method is the transmission experiment. Here one measures the intensity of particles before and after the target and infers the total cross section from the relation

$$I = I_0 \exp(-N\sigma_T) \tag{15.11}$$

where I (I_0) is the transmitted (incident) intensity and N is the number of target nuclei/cm^2. This method is frequently employed at fixed target accelerators. We will also mention several methods of extracting the total cross section from the measurements of small angle elastic scattering in Section 15.3.

As an example of the first method, we consider a measurement of the pp total cross section at the CERN ISR [13]. The apparatus shown in Fig. 15.7 consists of two large scintillator hodoscopes surrounding each of the beam pipes leaving the intersection region. The intersection point itself was sandwiched above and below by two large streamer chambers. Lead oxide plates in the chambers aided in converting photons.

Most interactions were detected by coincidences between the hodoscopes in the two arms. The signals from the near and far hodoscopes were ORed to produce an ARM_i signal. The distribution of time differences between the arms showed a narrow central peak, corresponding mostly to true beam–beam events, plus smaller side peaks 18 ns before and after the central peak. These side peaks were due to coincidences with stray beam particles and were removed by placing a ± 10-ns time window around the central peak.

The observed coincidence rates were corrected for accidentals, beam–gas collisions, and collisions with material near the intersection point. The streamer chambers were used to measure corrections necessary for events that triggered only one or neither of the hodoscope arms. Finally, for some

events, such as small angle elastic or single diffraction scattering, the particles remain in the beam pipe and are not detected. The rates for these processes had to be calculated from other measurements.

The luminosity was measured using the "Van de Meer method." This involves measuring the interaction rate as a function of the vertical displacement of the two beams relative to each other. The results of this experiment confirmed the rising value of the total cross section in the region $\sqrt{s} = 24-63$ GeV.

The second method of measuring the total cross section is the transmission experiment [14, 15]. A schematic of an idealized transmission experiment is given in Fig. 15.8. The incoming beam passes first through the

Figure 15.7 Apparatus for a total cross section measurement at the ISR. (H) Scintillator hodoscope and (SC) streamer chamber. (After K. Eggert et al., Nuc. Phys. B 98: 93, 1975.)

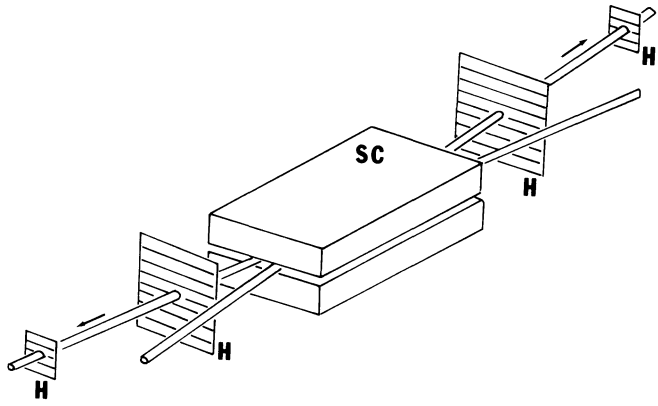

Figure 15.8 The "good-geometry" transmission arrangement for measuring the total cross section. (B) Incident beam counters, (T) target, and (F) transmission counters.

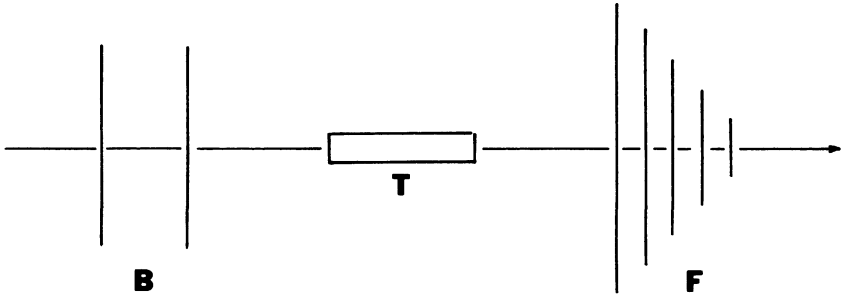

counters B and then the target T. Some of the incident particles will have a nuclear interaction in the target, while others will not. The total cross section is related to the total rate I for particles that do not interact by

$$\sigma_T = \frac{1}{N} \ln\left(\frac{I_0}{I}\right) \tag{15.12}$$

Ideally one would like to have an infinitesimal detector that can measure every noninteracting particle. However, even if this were possible, it would lead to errors, since the beam has a finite size, and since particles that traverse the target without a nuclear interaction may still undergo multiple scattering in the target material.

The finite size of the transmission counters leads to a new difficulty. Particles may undergo small angle nuclear elastic or diffraction scattering and yet remain inside the acceptance of the transmission counter. For this reason, a series of transmission counters are used, each subtending a different solid angle. The effects of beam size and multiple scattering are only important at small solid angles. Away from this region the transmitted intensity has the form

$$I = I_0 e^{-N\sigma_T}\left[1 + N\int_0^{\Omega} \frac{d\sigma}{d\Omega}\, d\Omega\right] \tag{15.13}$$

Thus an extrapolation of the finite solid angle data to zero solid angle gives the cross section with the small angle scattering properly accounted for.

As an example, consider the experiment of Citron et al. [16], which used the transmission method at the AGS to measure the $\pi^{\pm}$p total cross sections. The incoming beam intensity was measured using coincidences between three scintillation counters and a threshold Cerenkov counter. Data were taken with a liquid hydrogen target in the beam path. Empty target corrections were made by mounting an identical chamber on the same frame. The frame rolled on rails, so that either target could easily be placed in the beamline.

Seven circular transmission counters were used, subtending solid angles between 2 and 30 msr. The counters were arranged so that the radii decreased along the beam path. This arrangement permitted a determination of the statistical error on the difference between two adjacent cross section measurements and made the reduction in efficiency of later counters due to absorption the same for the target empty and target full runs.

Additional logic was used to measure the rate of accidental and circuit deadtime. Muon contamination in the pion beam was vetoed using an iron absorber and scintillator behind the transmission counters. Final

corrections were necessary to remove contributions to the measured cross sections from electromagnetic processes.

15.3 Elastic scattering

Elastic scattering has been used for many years as an aid in understanding the effective size or any internal structure of particles. The measured elastic cross section is actually the sum of nuclear scattering events, electromagnetic Coulomb scattering, and scattering due to the interference of the electromagnetic and nuclear amplitudes

$$\frac{d\sigma}{dt} = \frac{d\sigma_{\text{nuc}}}{dt} + \frac{d\sigma_{\text{Coul}}}{dt} + \frac{d\sigma_{\text{int}}}{dt} \tag{15.14}$$

For small angles the nuclear differential cross section has an approximately exponential dependence on t

$$\frac{d\sigma_{\text{nuc}}}{dt} = A \exp(bt) \tag{15.15}$$

where A is the nuclear differential cross section at $t = 0$ and b is the slope parameter. Sometimes it is more interesting to examine the local slope, defined by

$$b(t) = \frac{d}{dt}\left(\ln \frac{d\sigma}{dt}\right) \tag{15.16}$$

The total cross section may be determined from elastic scattering measurements by using the optical theorem [14, 17]

$$\sigma_{\text{T}}^2 = \frac{16\pi A}{1+\rho^2} \tag{15.17}$$

where ρ is the ratio of the real to imaginary part of the forward nuclear elastic scattering amplitude.

The Coulomb scattering cross section is the square of the amplitude [14]

$$C = \frac{2\alpha}{|t|} G^2(t) e^{i\alpha\phi(t)} \tag{15.18}$$

where $G(t)$ is the particle form factor, $\phi(t)$ is the phase of the Coulomb amplitude, and α is the fine structure constant. The form factor is related to the electromagnetic structure of the particle. The interference cross section is

$$\frac{d\sigma_{\text{int}}}{dt} = -2[\rho + \alpha\phi(t)] \frac{2\alpha}{|t|} G^2(t) \sqrt{\frac{A}{1+\rho^2}}\, e^{1/2(bt)} \tag{15.19}$$

https://doi.org/10.1017/9781009290098.016 Published online by Cambridge University Press

It is important to note that near $t = 0$ the Coulomb cross section goes like $1/t^2$, while the interference cross section goes like $1/t$.

We consider as an example the high energy elastic scattering measurement of Schiz et al. [18] at Fermilab. The experimenters measured the πp and pp elastic differential cross sections at 200 GeV/c for the t interval $0.02 < t < 0.66$ GeV^2. Figure 15.9 shows the experimental arrangement. The incoming beam particles were identified using four Cerenkov counters. Two groups of high resolution PWCs were used on each side of the liquid hydrogen target to measure the scattering angle. The forwardly scattered beam was focused onto a plane downstream of the spectrometer magnet. A scintillation counter located there vetoed unscattered tracks. Another set of PWCs following the magnet measured the bend angle.

The experiment used a two-level trigger. The first level, which came from the scintillators, essentially required a good beam track, together with a signal at the end of the forward arm, and no veto. This trigger was dominated by beam halo particles, so a higher level was also employed using information from the PWCs. A hardware device required that the trajectory intercept a preset window in the veto plane and that the projected scattering angle exceed $-t = 0.01$ GeV^2. Special "beam" triggers were also collected for alignment and normalization, and some first-level triggers were taken to study the efficiency and biases of the hardware trigger device.

A number of cuts were applied to the raw data to eliminate unusable tracks and to help extract the elastic signal. The data was grouped into bins of $q = \sqrt{-t} \simeq p_b\theta$, where p_b is the beam momentum and θ is the scattering angle. The number of scatters in each bin $N_s(q)$ was then determined by

Figure 15.9 Experimental arrangement for measurement of high energy elastic scattering. (C) Cerenkov counter, (P) MWPC, (t) target, (M) bending magnets, (V) veto counter, and (S) trigger scintillator. (After A. Schiz et al., Phys. Rev. D 24: 26, 1981.)

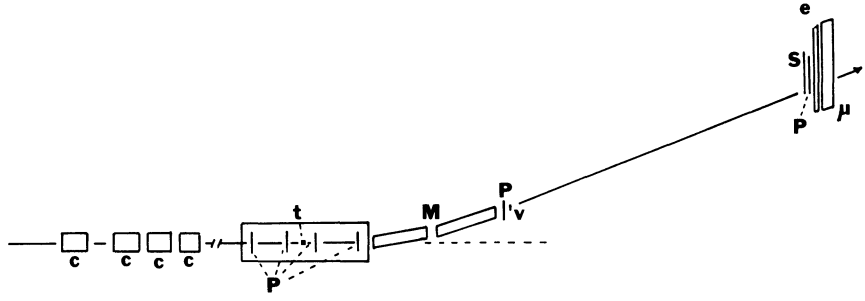

https://doi.org/10.1017/9781009290098.016 Published online by Cambridge University Press

making a normalized, target empty subtraction from the measured events.

The data had to be corrected for several effects. First, radiation of photons by the scattered particles may cause a good elastic event to be missed. Thus a correction factor C_{rad} was calculated that was largest (8%) for large q pions. Second, the measured data still contained some inelastic contamination. A factor C_{in} was determined by fitting the recoil mass distribution to a peak at the proton mass plus background as shown in Fig. 15.10. The largest corrections (9%) occurred for high q proton events. A third correction C_{pl} was necessary to account for events with two nuclear scatters in the target. These events incorrectly enhance the large q bins.

The total elastic cross section may be determined by integrating the measured $d\sigma/dt$ over t. The data must be extrapolated for the regions of t not measured. There is a check on the extrapolation at $t = 0$ from the optical theorem. The measured pp elastic cross section at 200 GeV/c accounts for almost 18% of the total cross section.

15.4 Polarization experiments

It has become increasingly clear that spin dependent interactions remain important up to the highest available accelerator energies [19]. For reactions where one or both of the initial or final state particles has nonzero spin, there are many spin dependent observables in addition to

Figure 15.10 Recoil mass distribution in an elastic scattering experiment. (After A. Schiz et al., Phys. Rev. D 24: 26, 1981.)

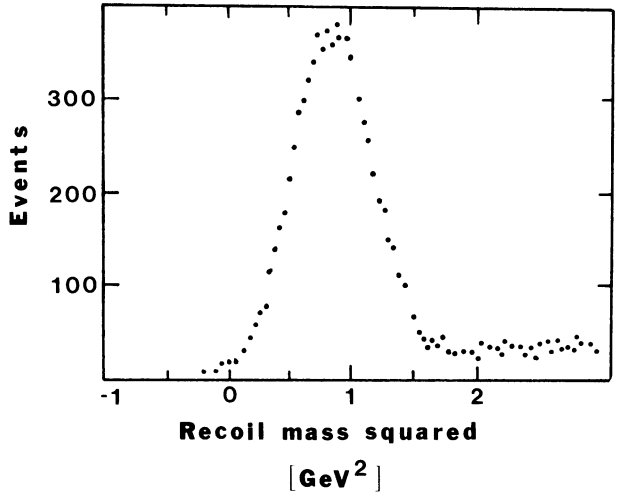

https://doi.org/10.1017/9781009290098.016 Published online by Cambridge University Press

the ordinary spin-averaged differential cross section. Remarkable structure has been observed in some of these observables, for example, the two particle asymmetries in pp elastic scattering.

The simplest of the spin dependent observables is the analyzing power $\mathscr{A}$. Consider the elastic scattering of a spin 0 beam particle from a spin $\frac{1}{2}$ target particle. If we denote by N_L (N_R) the fraction of the events in which the fast forward particle scatters at an angle θ to the left (right), then the analyzing power is defined by

$$\mathscr{A} = \frac{1}{P_T} \frac{N_L - N_R}{N_L + N_R} \tag{15.20}$$

where P_T is the average polarization of the target particles. Note that $\mathscr{A}$ is a function of the angle θ and of the particle's momentum. To measure $\mathscr{A}$ in this way would require two forward spectrometers. However, the same quantity $\mathscr{A}$ can be obtained by using one spectrometer at an angle θ, to the left say, and instead taking data with the target polarization in opposite directions. Then $\mathscr{A}$ is given by

$$\mathscr{A} = \frac{1}{P_T} \frac{N_+ - N_-}{N_+ + N_-} \tag{15.21}$$

where N_+ (N_-) is the fraction of events with the target polarized up (down). Because of the expense of building a second spectrometer and the ease of reversing the target polarization, most high energy experiments are performed this way. The analyzing power is sometimes referred to as the asymmetry or polarization parameter.

Measurements of observables that only involve initial state polarizations are readily performed if a polarized beam and a polarized target are available. The polarization of final state particles can be measured by scattering them off a secondary target, such as carbon. However, the requirement for double scattering makes measurements of observables that involve final state polarizations much less precise than those that only involve the initial state. Table 15.1 lists some of the observables that have been measured in spin 0 – spin $\frac{1}{2}$ and spin $\frac{1}{2}$ – spin $\frac{1}{2}$ 2-body scattering. The table uses the 2-body to 2-body scattering notation of Chapter 1. The various observables are classified depending on whether the initial state particles have been prepared with a net polarization and whether the polarization of final state particles is analyzed along some direction. The polarization of the fast forward, final state particles (1) is usually not analyzed because this requires rescattering the fast particles from a secondary target, and the value of the analyzing power of most substances at high energies is quite small. Many of the components of the observables in

Table 15.1 are either 0 or are related to each other because of symmetry principles.

The analysis of polarized target data is complicated by the fact that only the protons in hydrogen atoms in the target material are polarized. The remaining ~90% of the target nuclei contained mostly in carbon and oxygen atoms are not polarized. This nonpolarized background is reduced for the case of elastic scattering. The nuclei in the heavier atoms have a Fermi momentum distribution, which makes it more difficult for events from those atoms to satisfy the elastic correlations. To determine the background under the elastic signal coming from these unpolarized nuclei, special runs can be taken using carbon or Teflon targets.

Consider as an example the measurements by the SLAC–Yale group [20, 21] of polarized electron-polarized proton scattering at the SLAC linac. The experiment was designed to explore the internal spin structure of the proton using a polarized electron probe, in analogy with the classic series of experiments that used (unpolarized) electrons to study the spatial structure of the proton.

Table 15.1. *Summary of spin 0–spin $\frac{1}{2}$ and spin $\frac{1}{2}$–spin $\frac{1}{2}$ observables*

	Particle[a]			
Observable	b	t	1	2
Spin 0–spin $\frac{1}{2}$				
σ_0	np	np	na	na
A_i	np	p	na	na
P_i	np	np	na	a
D_{ij}	np	p	na	a
Spin $\frac{1}{2}$–spin $\frac{1}{2}$				
σ_0	np	np	na	na
A_i	p	np	na	na
A_i	np	p	na	na
A_{ij}	p	p	na	na
P_i	np	np	na	a
C_{ij}	np	np	a	a
D_{ij}	np	p	na	a
K_{ij}	p	np	na	a
H_{ijk}	p	p	na	a

[a]Abbreviations: p, initial state particle is polarized along one of three orthogonal directions; np, initial state particle is not polarized; a, component of polarization of final state particle is analyzed along one of three orthogonal directions; na, polarization of final state particle is not analyzed.

The overall layout of the experiment is shown in Fig. 15.11. A longitudinally polarized electron beam strikes a longitudinally polarized proton target, and any outgoing electrons are identified and measured inclusively in the forward spectrometer. In order to obtain the polarized beam, a polarized electron source had to be installed on the linac. The source used ultraviolet light to photoionize a beam of ^{6}Li atoms in which the electrons were strongly polarized. The direction of the polarization was either parallel or antiparallel to the electron momentum, depending on the direction of the current in the polarizing coils. The polarization was frequently reversed to minimize systematic errors. The polarization of the beam leaving the source was measured by double Mott scattering of a portion of the beam on a gold foil. The polarization of the accelerated high energy beam was measured by elastic (Moller) scattering from a magnetized iron foil. The beam had an average intensity of 5×10^8 electrons/pulse and a polarization of 80%.

The incoming electron beam interacted in a polarized proton target located in the 5-T field of a superconducting solenoid. The actual target material consisted of frozen beads of butanol doped with the organic free radical porphyrexide. The target was maintained at a temperature of 1 K using a ^{4}He evaporation cryostat. The polarization of the free protons in the target averaged 60%. This was measured by surrounding the target with the coil of a NMR circuit. Radiation damage from the electron beam caused serious depolarization in the target. In order to minimize this effect and to ensure uniform polarization, the beam was rastered quickly across the target. In addition, techniques had to be developed to anneal away some of target damage and to quickly change the target material.

The forward spectrometer used two large dipole bending magnets and a

Figure 15.11 Schematic of the SLAC polarized electron-polarized proton scattering experiments. (PeB) Polarized electron beam, (PPT) polarized proton target, (M) bending magnet, (C) Cerenkov counter, (W) MWPC, (H) hodoscope, and (LG) lead-glass shower counter.

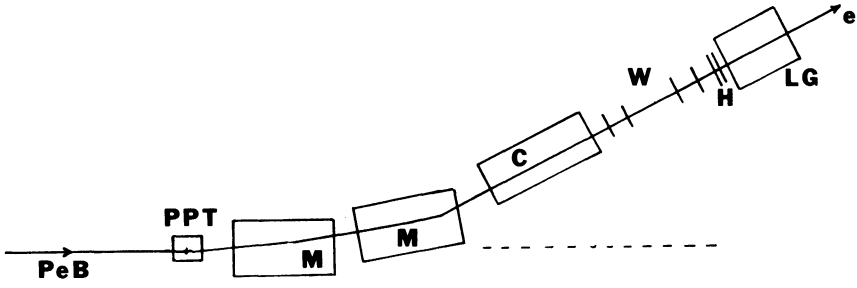

https://doi.org/10.1017/9781009290098.016 Published online by Cambridge University Press

4000-wire set of PWCs for particle tracking. The outgoing electrons were identified using a 4-m-long gas threshold Cerenkov counter and a segmented lead-glass shower counter.

The measured asymmetry averaged over the target polarization is

$$\Delta = \frac{N_+ - N_-}{N_+ + N_-}$$

where N_+ and N_- are the normalized event rates when the electron has positive and negative helicity, respectively. The measured asymmetry was very small ($\sim 1\%$). For this reason careful attention had to be paid to minimizing possible systematic errors due to variations in the intensity, position, or direction of the beam. The measured asymmetry is related to the intrinsic asymmetry A associated with polarized ep scattering by

$$\Delta = P_e P_p f A \tag{15.22}$$

where P_e and P_p are the electron and proton polarization and f is the fraction of free protons (hydrogen atoms) in the target.

The instrinsic asymmetry is a function of the variable $x = Q^2/2Mv$, where Q^2 is the relativistic 4-momentum transfer to the proton, v is the energy loss of the electron, and M is the mass of the proton. At large x the asymmetry becomes very large and positive. This is interpreted by QCD models to mean that the probability is large that a quark that carries a large fraction of the nucleon's momentum will also carry its spin.

15.5 New particle searches

Among the most satisfying and exciting experiments in physics are those that discover the existence of new particles. Sometimes the discovery was hoped for, yet still unexpected, as in the case of the J/ψ. This particle was discovered almost simultaneously in 1974 by a production experiment at the AGS at BNL and by a formation experiment at the SPEAR storage ring at SLAC. Other times fairly precise predictions exist for a particle state, but some combination of very high mass, small production cross section, or large background conspire to make the experimental measurement very difficult. This was the case for the W gauge bosons, which were discovered in 1983 by two groups at the CERN SPS $\bar{p}p$ collider.

First let us consider the classic experiment of Samuel Ting and collaborators, who discovered the J half of the J/ψ particle [22, 23]. Ting was interested in searching for possible high mass vector mesons. These strongly interacting particles have the same quantum numbers as the photon. Any such particle should decay into e^+e^- pairs. However, the

https://doi.org/10.1017/9781009290098.016 Published online by Cambridge University Press

branching ratio for e^+e^-, which comes from electromagnetic processes, should be much smaller than that for pairs of hadrons. In addition, the angular distribution of electromagnetic processes fall off very sharply. Thus, the experiment required a high resolution detector with good acceptance for e^+e^- pairs that could handle very high rates of beam particles and that had a very high rejection capability for hadron pairs.

A schematic of the experiment is shown in Fig. 15.12. A slow extracted beam from the AGS was focused onto a beryllium target. The incident beam intensity was $\sim 10^{12}$ protons/pulse. The spectrometer consisted of two identical arms. Each arm contained three bending magnets $M_0 - M_2$, two threshold Cerenkov counters C_0 and C_e, and a lead-glass shower counter S for particle identification, MWPCs for tracking, and scintillation counter hodoscopes. The downstream portion of the arms were elevated by 10.33° in order to decouple the measurements of the particles' momenta and their production angles. The magnetic spectrometer had a mass resolution of ± 5 MeV and a mass acceptance of 2 GeV, making it ideally suited for searching over a large mass range for a narrow resonance.

The combination of Cerenkov and shower counters gave a rejection against hadron pairs by a factor $> 10^8$. The Cerenkov counter was filled with H_2 gas to minimize the production of knock-on electrons. The counters were separated by a magnetic field so that the electrons produced in the first counter would not be detected by the second.

Figure 15.12 Double arm spectrometer for high mass electron pairs. (T) Target, (M_0, M_1, M_2) bending magnets, (C_0, C_e) Cerenkov counters, (S) lead-glass and shower counters. The C_B Cerenkov counter was located below M_0 and is not shown. (After S.C.C. Ting, Rev. Mod. Phys. 49: 235, 1977.)

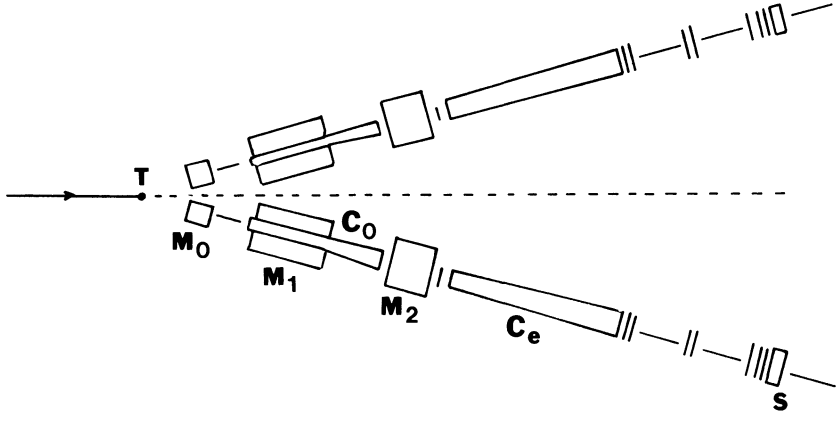

https://doi.org/10.1017/9781009290098.016 Published online by Cambridge University Press

The system was calibrated using electrons from the decay $\pi^0 \rightarrow \gamma e^+ e^-$. One of the e^+ or e^- particles was tagged with a highly directional Cerenkov counter (not shown) close to the target, while the other particle went through the spectrometer. The experimental e^+e^- mass spectrum near 3 GeV is shown in Fig. 15.13. The J/ψ resonance stands out clearly above a small background of nonresonant and misidentified events. The dotted histogram represents data taken at a lower magnet current. It is one of

Figure 15.13 Mass spectrum for electron pairs. The bin width is 25 MeV. The dotted spectrum was collected with the spectrometer magnet running at a reduced current. (After S.C.C. Ting, Rev. Mod. Phys. 49: 235, 1977.)

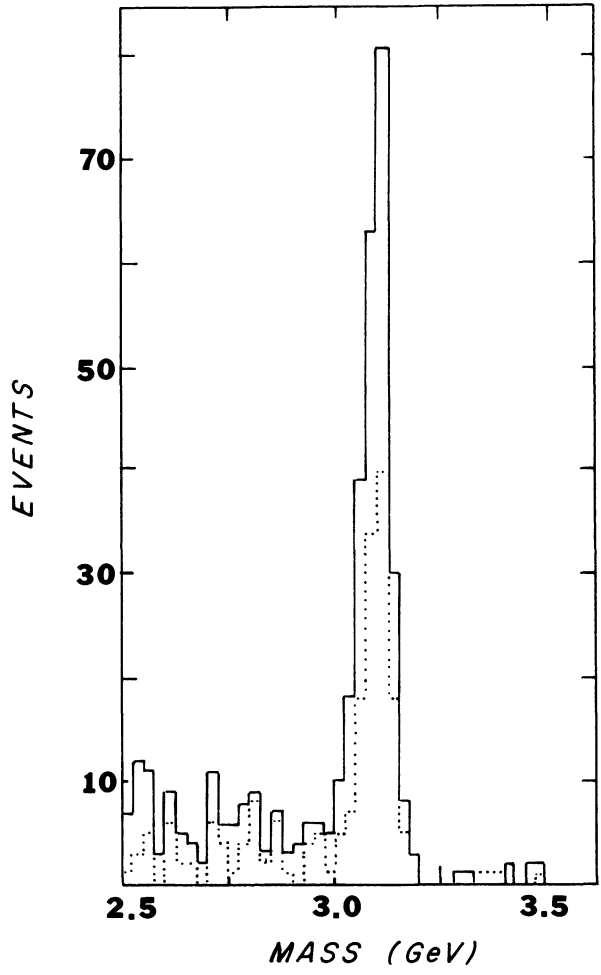

https://doi.org/10.1017/9781009290098.016 Published online by Cambridge University Press

many checks that the peak was not due to an instrumental effect. Lowering the current causes the particle to traverse different portions of the spectrometer and would presumably shift any effect caused by the apparatus itself.

Lastly, let us mention the discovery of the charged W vector bosons by a group headed by Carlo Rubbia at CERN [24]. The highly successful electroweak theory had predicted that the mass of the W should be around 82 GeV. The W was predicted to decay via

$$W^{\pm} \longrightarrow e^{\pm}\nu$$

with a significant branching ratio, so the experiment was designed to search for the production of electrons and neutrinos. In order to reach the very high CM energies where such massive particles could be produced, a large project was initiated at CERN to convert the SPS to a $\bar{p}p$ collider. An elaborate $\bar{p}$ cooling scheme similar to that discussed in Chapter 4 was devised by Van de Meer and coworkers in order to get the luminosity up to useful levels.

The UA1 detector at the SPS is shown in Fig. 15.14. The interaction point is surrounded by a central detector, which consists of a cylindrical drift chamber 5.8 m long and 2.3 m in diameter. The central detector sits in a 0.7-T dipole field. The typical momentum resolution is 20% for a 1-m-long, 40-GeV/c particle. The central detector was used to determine the overall topology of the event and to measure the charge and momentum of electron candidates. Electrons were identified by a large energy deposit in the lead–scintillator electromagnetic calorimeter and by the lack of penetration into the iron–scintillator hadron calorimeter. The electromagnetic shower counters were 27 radiation lengths deep and had an energy resolution of $15\%/\sqrt{E}\,(\text{GeV})$. The electromagnetic calorimeters extended over 99% of 4π, so that the neutrino could be identified through an unbalance in the visible energy flow transverse to the beam axis. Since muons were capable of carrying substantial amounts of energy outside of the calorimeters, the detector was surrounded by eight layers of proportional drift tubes.

The trigger required at least 10 GeV of transverse energy in two electromagnetic calorimeter elements. The trigger rate was 0.2 events/sec at a luminosity of $5 \times 10^{28}\ \text{cm}^{-2}\ \text{s}^{-1}$. Two parallel analyses were used on the final sample of high quality events with associated vertices in the central detector. The first analysis examined charged tracks for clean, isolated electrons. A second independent analysis looked at the calorimeter information for events with missing transverse energy. With a few exceptions

Figure 15.14 The UA1 detector at CERN. (Courtesy of the UA1 collaboration and the Particle Data Group.)

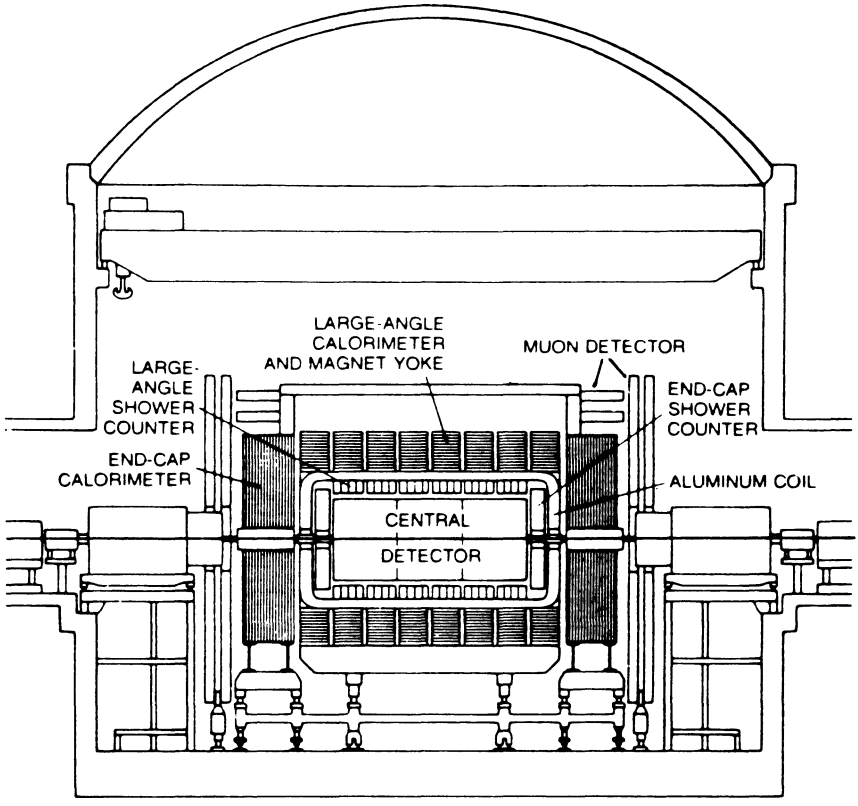

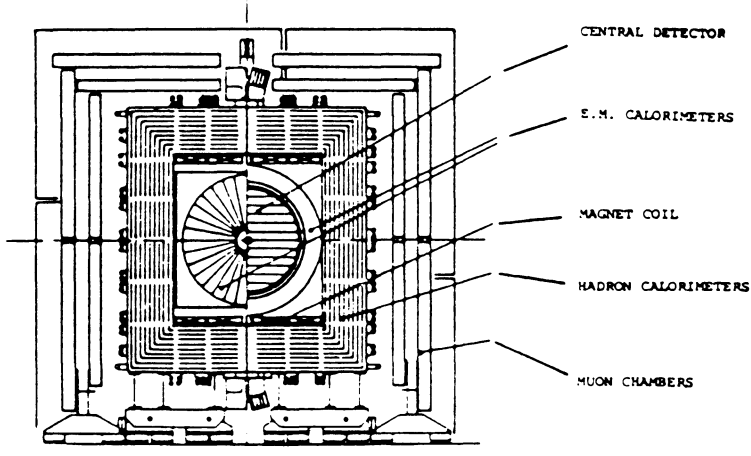

https://doi.org/10.1017/9781009290098.016 Published online by Cambridge University Press

both analyses led to the same set of final events. Figure 15.15 shows the association of the missing transverse momentum for the electron candidate events. The missing energy lies antiparallel to the electron direction, suggesting a 2-body decay. Assuming that these events are the decay products of the W, and taking the W decay kinematics and transverse momentum of the W at production into account, the data gave $m_W = 80.9 \pm 1.5$ GeV, in excellent agreement with the theoretical predictions.

The UA1 experiment illustrates two important points concerning experiments at the multi-TeV accelerators now under consideration. First is the increasing difficulty in using magnetic spectrometers. The high energy events are characterized by very large multiplicities of charged particles. It becomes more and more difficult to pattern-recognize the tracks of all these particles and to accurately measure their momenta. The second feature is the increasing importance of finely segmented, good resolution calorimeters. The measurement of vector energy flow is a very powerful tool for examining the new physics of jets and high mass particle states.

Figure 15.15 Components of the missing transverse energy are plotted relative to the electron direction. (After G. Arnison et al., Phys. Lett. 129B: 273, 1983.)

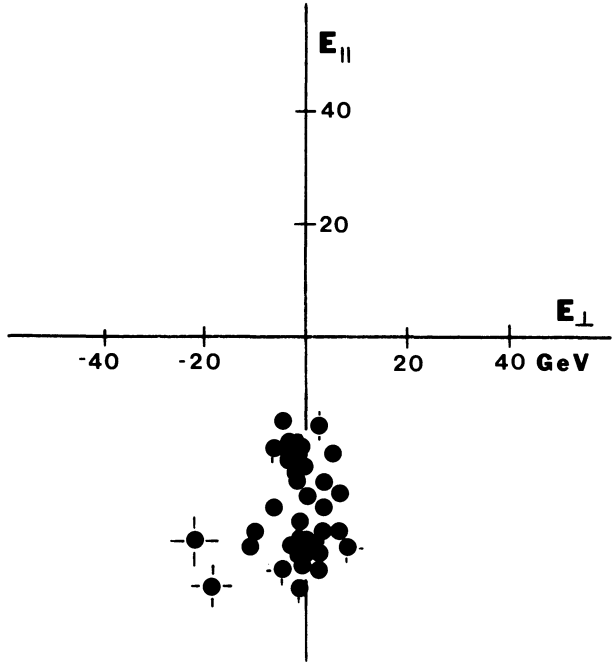

https://doi.org/10.1017/9781009290098.016 Published online by Cambridge University Press

References

[1] A. Marini, I. Peruzzi, M. Piccolo, F. Ronga, D.M. Chew, R.P. Ely, T.P. Pun, V. Vuillemin, R. Fries, B. Gobbi, W. Guryn, D.H. Miller, M.C. Ross, D. Besset, S.J. Freedman, A.M. Litke, J. Napolitano, T.C. Wang, F.A. Harris, I. Karliner, S. Parker, and D.E. Yount, Search for exclusive free-quark production in e^+e^- annihilation, Phys. Rev. Lett. 48: 1649–52, 1982.

[2] R. Seki and C. Wiegand, Kaonic and other exotic atoms, Ann. Rev. Nuc. Sci 25: 241–81, 1975.

[3] F. Farley and E. Picasso, The muon (g-2) experiments, Ann. Rev. Nuc. Sci 29: 243–82, 1979.

[4] G. Kallen, *Elementary Particle Physics,* New York: Addison-Wesley, 1964, Chap. 2.

[5] M. Daum, G. Eaton, R. Frosch, H. Hirschmann, J. McCulloch, R. Minehart, and E. Steiner, Precision measurement of the muon momentum in pion decay at rest, Phys. Rev. D 20: 2692–707, 1979; final results obtained with an improved apparatus are given in R. Abela, M. Daum, G. Eaton, R. Frosch, B. Jost, P. Kettle, and E. Steiner, Precision measurement of the muon momentum in pion decay at rest, Phys. Lett. 146B: 431–6, 1984.

[6] L. Yuan and C. Wu, *Methods of Experimental Physics,* Vol. 5, Part B, New York: Academic, 1963, Sec 2.4.

[7] D. Perkins, *Introduction to High Energy Physics,* New York: Addison-Wesley, 1972, pp. 79–83.

[8] The form we use here is from B. Montague, Elementary spinor algebra for polarized beams in storage rings, Part. Accel. 11: 219–31, 1981.

[9] F. Combley, F. Farley, and E. Picasso, The CERN muon (g-2) experiments, Phys. Rep. 68: 93–119, 1981.

[10] L. Schachinger, G. Bunce, P. Cox, T. Devlin, J. Dworkin, B. Edelman, R. Edwards, R. Handler, K. Heller, R. March, P. Martin, O. Overseth, L. Pondrom, M. Sheaff, and P. Skubic, Precise measurement of the Λ magnetic moment, Phys. Rev. Lett. 41: 1348–51, 1978.

[11] M. Bourquin, R.M. Brown, J.C. Chollet, A. Degre, D. Froidevaux, J.M. Gaillard, C.N.P. Gee, J.P. Gerber, W.M. Gibson, P. Igo-Kemenes, P.W. Jeffreys, M. Jung, B. Merkel, R. Morand, H. Plothow-Besch, J.P. Repellin, J.L. Riester, B.J. Saunders, G. Sauvage, B. Schiby, H.W. Siebert, V.J. Smith, K.P. Streit, R. Strub, J.J. Thresher, and S.N. Tovey, Measurement of Ω^- decay properties in the CERN SPS hyperon beam, Nuc. Phys. B 241: 1–47, 1984.

[12] M. Schardt, J. Frank, C. Hoffman, R. Mischke, D. Moir, and P. Thompson, New measurement of the Dalitz-decay branching ratio of the π^0, Phys. Rev. D 23: 639–48, 1981.

[13] K. Eggert, H. Frenzel, K. Giboni, W. Thome, B. Betev, P. Darriulat, P. Dittmann, M. Holder, K. McDonald, H. Pugh, T. Modis, K. Tittel, V. Eckardt, H. Gebauer, R. Meinke, O. Sander, and P. Seyboth, A measurement of the proton-proton cross section at the CERN ISR, Nuc. Phys. B98: 93–9, 1975.

[14] G. Giacomelli, Total cross sections and elastic scattering at high energies, Phys. Rep. 23: 123–235, 1976.

[15] U. Amaldi, T. Fazzini, G. Fidecaro, C. Ghesquiere, M. Legros, and H. Steiner, Antiproton-proton total cross sections between 0.575 and 5.35 GeV/c, Nuovo Cimento 34: 825–53, 1964.

[16] A. Citron, W. Galbraith, T. Kycia, B. Leontic, R. Phillips, A. Rousset, and P. Sharp, Structure in the pion-proton total cross section between 2 and 7 GeV/c, Phys. Rev. 144: 1101–14, 1966.

[17] L. Fajardo, R. Majka, J. Marx, P. Nemethy, L. Rosselet, J. Sandweiss, A. Schiz, A. Slaughter, C. Ankenbrandt, M. Atac, R. Brown, S. Ecklund, P. Gollon, J. Lach, J. MacLachlan, A. Roberts, and G. Shen, Real part of the forward elastic nuclear amplitude for $\bar{p}p$, pp, π^+p, π^-p, K^+p, and K^-p scattering between 70 and 200 GeV/c, Phys. Rev. D 24: 46–65, 1981.

[18] A. Schiz, L. Fajardo, R. Majka, J. Marx, P. Nemethy, L. Rosselet, J. Sandweiss, A. Slaughter, C. Ankenbrandt, M. Atac, R. Brown, S. Ecklund, P. Gollon, J. Lach, J. MacLachlan, A. Roberts, and G. Shen, High statistics study of π^+p, π^-p, and pp elastic scattering at 200 GeV/c, Phys. Rev. D 24: 26–45, 1981.

[19] R. Fernow and A. Krisch, High energy physics with polarized proton beams, Ann. Rev. Nuc. Part. Sci. 31: 107–44, 1981.

[20] G. Baum, M.R. Bergstrom, P.R. Bolton, J.E. Clendenin, N.R. DeBotton, S.K. Dhawan, Y.-N. Guo, V.-R. Harsh, V.W. Hughes, K. Kondo, M.S. Lubell, Z.-L. Mao, R.H. Miller, S. Miyashita, K. Morimoto, U.F. Moser, I. Nakano, R.F. Oppenheim, D.A. Palmer, L. Panda, W. Raith, N. Sasao, K.P. Schuler, M.L. Seely, P.A. Souder, S.J. St. Lorant, K. Takikawa, and M. Werlen, New measurement of deep inelastic e-p asymmetries, Phys. Rev. Lett. 51: 1135–8, 1983.

[21] V. Hughes and J. Kuti, Internal spin structure of the nucleon, Ann. Rev. Nuc. Part. Sci. 33: 611–44, 1983.

[22] J.J. Aubert, U. Becker, P.J. Biggs, J. Burger, M. Chen, G. Everhart, P. Goldhagen, J. Leong, T. McCorriston, T.G. Rhoades, M. Rohde, S.C.C. Ting, S.L. Wu, and Y.Y. Lee, Experimental observation of a heavy particle J, Phys. Rev. Lett. 33: 1404–6, 1974.

[23] S.C.C. Ting, The discovery of the J particle: A personal recollection, Rev. Mod. Phys. 49: 235–49, 1977.

[24] G. Arnison, A. Astbury, B. Aubert, C. Bacci, G. Bauer, A. Bezaguet, R. Bock, T.J.V. Bowcock, M. Calvetti, T. Carroll, P. Catz, P. Cennini, S. Centro, F. Ceradini, S. Cittolin, D. Cline, C. Cochet, J. Colas, M. Corden, D. Dallman, M. DeBeer, M. Della Negra, M. Demoulin, D. Denegri, A. DiCiaccio, D. DiBitonto, L. Dobrzynski, J.D. Dowell, M. Edwards, K. Eggert, E. Eisenhandler, N. Ellis, P. Erhard, H. Faissner, G. Fontaine, R. Frey, R. Fruhwirth, J. Garvey, S. Geer, C. Ghesquiere, P. Ghez, K.L. Giboni, W.R. Gibson, Y. Giraud-Heraud, A. Givernaud, A. Gonidec, G. Grayer, P. Gutierrez, T. Hansl-Kozanecka, W.J. Haynes, L.O. Hertzberger, C. Hodges, D. Hoffmann, H. Hoffmann, D.J. Holthuizen, R.J. Homer, A. Honma, W. Jank, G. Jorat, P.I.P. Kalmus, V. Karimaki, R. Keeler, I. Kenyon, A. Kernan, R. Kinnunen, H. Kowalski, W. Kozanecki, D. Kryn, F. Lacava, J-P. Laugier, J.P. Lees, H. Lehmann, K. Leuchs, A. Leveque, D. Linglin, E. Locci, M. Loret, J-J. Malosse, T. Markiewicz, G. Maurin, T. McMahon, J-P. Mendiburu, M-N. Minard, M. Moricca, H. Muirhead, F. Muller, A.K. Nandi, L. Naumann, A. Norton, A. Orkin-Lecourtois, L. Paoluzi, G. Petrucci, G. Piano Mortari, M. Pimia, A. Placci, E. Radermacher, J. Ransdell, H. Reithler, J-P. Revol, J. Rich, M. Rijssenbeek, C. Roberts, J. Rohlf, P. Rossi, C. Rubbia, B. Sadoulet, G. Sajot, G. Salvi, G. Salvini, J. Sass, J. Saudraix, A. Savoy-Navarro, D. Schinzel, W. Scott, T.P. Shah, M. Spiro, J. Strauss, K. Sumorok, F. Szoncso, D. Smith, C. Tao, G. Thompson, J. Timmer, E. Tscheslog, J. Tuominiemi, S. Van der Meer, J-P. Vialle, J. Vrana, V. Vuillemin, H.D. Wahl, P. Watkins, J. Wilson, Y.G. Xie, M. Yvert, and E. Zurfluh, Experimental observation of isolated large transverse energy electrons with associated missing energy at $\sqrt{s} = 540$ GeV, Phys. Lett. 122B: 103–16, 1983; Further evidence for charged intermediate vector bosons at the SPS collider, Phys. Lett. 129B: 273–82, 1983.

Exercises

1. Calculate the net precession angle of a 40-GeV/c Λ crossing a 2-m-long, 1-T magnetic field? What is the net precession angle for a 40-GeV/c Σ^-?
2. What is the fractional loss of intensity for a 30-GeV/c proton beam passing through a 25-cm-long liquid hydrogen target?
3. Calculate the value of $d\sigma/dt$ at $t = 0$ for pp elastic scattering between 10 and 100 GeV/c using total cross section measurements. Ignore the real part of the forward amplitude.
4. A polarization experiment uses a polarized pentanol target with polarization 50% and a 60% polarized beam. What is the intrinsic asymmetry of the physical process if 1000 events are measured with the target polarized up and 1040 events are measured with it polarized down?

The following exercises require the reader to go through some of the steps involved in writing a proposal. Find references to the original literature in the Particle Data Tables. Using previously measured values, theory, or reasonable guesses, estimate the cross sections for any relevant processes. Give the required beam energy and intensity, target material and dimensions, and amount of time required for data taking. Specify the detector characteristics, sketch their arrangement, and estimate the acceptance. Give the trigger and possible background processes. Consider possibles inefficiencies that could lead to a loss of events. Estimate the final number of good events and the accuracy of any measurements.

5. Prepare a proposal to search for free quarks at the Tevatron $\bar{p}p$ collider.
6. Prepare a proposal to lower the upper limit on the measurement of the branching ratio for $K^0 \rightarrow e\mu$.
7. Prepare a proposal to study the charged decay modes of the E meson using a K^- beam.

https://doi.org/10.1017/9781009290098.016 Published online by Cambridge University Press